Electrohydrodynamics of a liquid drop in confined domains

Asghar Esmaeeli* and Ali Behjatian
Department of Mechanical Engineering & Energy Processes, Southern Illinois University, Carbondale, Illinois 62901, USA
(Received 17 May 2012; revised manuscript received 26 July 2012; published 17 September 2012)

The steady-state electrohydrodynamics of a leaky dielectric drop in confined domains is investigated analytically. The governing electrohydrodynamic equations are solved for Newtonian and immiscible fluids in the framework of leaky dielectric theory and for the creeping flow regime. The domain confinement strengthens or weakens the electric field, depending on $R > 1$ or $R < 1$, respectively, where $R = \sigma_i/\sigma_o$ is the ratio of electric conductivity of the drop to that of the surrounding fluid. Similarly, the flow intensity decreases for $R < 1$, but it remains unchanged or increases for $R > 1$, depending on the interplay of electric and hydrodynamic effects. An expression for the drop deformation for small distortion from the spherical shape is found using the domain perturbation technique. It is shown that below a threshold domain size the confinement effect will lead to the reversal of the tendency of the net normal hydrodynamic stress in deforming the drop to an oblate or a prolate shape, and that below a critical domain size the necessary condition for having an oblate drop will be opposite to the classical one for an unbounded domain.

DOI: 10.1103/PhysRevE.86.036310 PACS number(s): 47.65.−d, 82.70.−y, 83.50.−v, 47.57.−s

I. INTRODUCTION

The behavior of a liquid drop in an externally applied electric field has been a problem of long-standing interest because of its relevance in a broad range of natural and industrial process. Examples include disintegration of rain drops in thunderstorm [1], electric breakdown of insulating dielectric liquids due to the presence of small water droplets [2], enhancement of heat and mass transfer [3,4], and enhanced coalescence and demixing in emulsions [5]. The electric field provides a well-known means for manipulation of the drops through induced interfacial stresses that can deform, burst, or set the drop in motion. Currently there is a renewed interest in the subject in the context of micro- and bio-fluidics applications, such as manipulation of droplets by continuous electrowetting (electrocapillarity) [6], protein transfection into cells by collision of droplets [7], and enhancement of heat and mass transfer by electric-field-driven chaotic mixing [8], to name a few.

Early analytical studies on the subject were done in the framework of "electrohydrostatic" theory [2,9–13], where the drop and the ambient fluid are treated as both being perfect dielectrics, or as a perfectly conducting fluid in a perfect dielectric fluid. In either case, the electrohydrostatic theory predicts that the "net" electric stress will be normal to the interface, pointing from the fluid of higher electric permittivity to the one with lower permittivity, and the drop will always elongate in the direction of the electric field, producing a prolate spheroid. Furthermore, since the theory entails continuity of tangential electric stress at the interface, it precludes the existence of fluid flow at the equilibrium. However, the experiments of Allan and Mason [11] for a wide range of fluid systems showed that conducting drops deformed into prolate spheroids, in agreement with the theory, while some perfect dielectric drops elongated in the direction perpendicular to the electric field, becoming an oblate spheroid. Motivated by the anomalous observations of Allan and Mason [11], Taylor [14] pointed out that interfacial hydrodynamic stresses are consequential for nonprolate deformation. To account for these stresses, therefore, the fluids should not be treated as perfect dielectrics; rather they should be considered as having slight conductivity to allow for accumulation of free charge at the interface. The action of electric field on this charge will then lead to an imbalance in the tangential interfacial electric stresses, which in turn leads to hydrodynamic interfacial shear stresses that must develop to balance the electrical shear stresses.

Taylor [14] solved the steady-state axisymmetric electrohydrodynamic equations for the fluids inside and outside of a spherical drop in the creeping flow regime. The domain was unbounded and an electric field $\mathbf{E}_\infty$, uniform at large distance, was applied to the drop. He showed that the relative importance of the ratios of electric conductivities $R = \sigma_i/\sigma_o$ and permittivities $S = \epsilon_i/\epsilon_o$, of the fluid in the drop to the ambient fluid, is the key parameter in setting the senses of drop deformation and fluid circulation. Specifically, he showed that the electric field establishes a circulatory flow in the drop, consisting of four vortices of equal strengths that are matched by counterpart vortices in the ambient fluid. For $R < S$, the direction of the ambient flow is from the poles (aligned in the direction of the electric field) to the equator, while for $R > S$ the flow direction is the opposite. For $R = S$, there is no fluid flow since the interface is free of charge. He also found a characteristic function Φ to predict the sense of the drop deformation. For $\Phi < 0$, the drop deforms to an oblate spheroid while for $\Phi > 0$ it deforms to a prolate spheroid. $\Phi = 0$ represents a zero deformation state which is a possibility for leaky dielectric fluids because of intricate interplay of electric and hydrodynamic stresses, despite the distorting effect of electric field.

Since the seminal work of Taylor [14], there have been several major analytical and numerical studies concerning the dynamics of a leaky dielectric drop. In what follows we only refer to the more relevant ones. The deformation of a drop $\mathcal{D}$ was calculated by Vizika and Saville [15] who used Taylor's solution [14] and balanced the normal stresses at the drop surface posteriorly. The authors used Taylor's

*Corresponding author: esmaeeli@engr.siu.edu

definition for deformation [16] and showed that the sense of deformation is set by the sign of the characteristic function Φ (found earlier by Taylor [14]) and its magnitude is linearly proportional to the square of the electric field strength E_∞^2. The effect of fluid inertia was studied by Tsukada *et al.* [17] who performed Galerkin finite element calculations and solved the momentum equations by accounting for the convective terms and compared their numerical results with Taylor's results and their own experiments. The authors showed that the linear $\mathcal{D}$-E_∞^2 relationship predicted by Taylor's asymptotic solution no longer holds as the electric field strength increases and inertia effect comes to picture. A comprehensive study on the effect of inertia was done by Feng and Scott [18] who used a Galerkin finite element method and examined the deformation of drops over a broad range of physical parameters. The authors showed that Taylor's asymptotic results tended to underestimate both the flow intensity and the drop deformation, and that significant differences existed between their computational predictions and that of asymptotic theory when the drop deformation became noticeable, even in the creeping flow limit. Furthermore, they found that a drop with oblate deformation at low electric field strength can evolve into a prolate shape as the field strength increases. In a follow-up study, Feng [19] explored the effect of convection of free charge at the interface. He concluded that the charge convection generally tends to reduce the intensity of the induced flow. Consequently, when the charge convection is accounted for, oblate drops will be less deformed compared to when the charge convection is ignored, while the opposite is true for the prolate drops. While at low electric field strengths a liquid drop settles to an equilibrium shape, it becomes unstable and even disintegrates beyond a critical electric field strength; see, for example, Refs. [1,2,11,12,20,21]. A noteworthy study in this regard was done by Sherwood [22] who investigated the response of a leaky dielectric drop in high electric fields using numerical simulations. More recent studies include the analytical work of Bentenitis and Kraus [23] who developed the so-called "extended leaky dielectric method" (ELDM) to study highly deformed drops in strong electric fields and the numerical simulations of Lac and Homsy who [24] extended Sherwood's work over a broader range of parameters.

While the steady-state electrohydrodynamics of a liquid drop in an unbounded domain is reasonably well understood, not much is known about the effect of domain confinement on the behavior of a drop. This understanding, however, finds relevance in microfluidic applications where the dimensions of the channel are typically of the same order as the drop size. Although from Taylor's [14] solution one can find an estimate of the minimum distance at which the confinement effect becomes insignificant, to understand the manner by which the results will be affected and for quantification purposes, one must incorporate the wall effects into the solution. The goal of this study is, therefore, to explore and quantify the effect of confinement on the drop deformation. To this end, we build on Taylor's solution and solve the electrohydrodynamic equations for a spherical liquid drop in a confined domain. We then evaluate the drop deformation for small distortion from the spherical shape using a domain perturbation technique.

The organization of the paper is as follows. In Sec. II, we discuss the problem setup and the governing nondimensional numbers. In Sec. III the governing electrohydrodynamic equations and their solution are presented. The drop deformation is evaluated in Sec. IV and in Sec. V the deformation-circulation map is discussed and the effect of confinement on this map is explored. Finally, in Sec. VI we conclude with a discussion of the findings.

II. PROBLEM SETUP AND NONDIMENSIONAL PARAMETERS

The problem setup is shown in Fig. 1, depicting a liquid drop of radius a suspended in another fluid and confined by a spherical rigid container of radius b. The drop and the container are concentric and the origin of the spherical coordinate system is at the center of the drop. Since the problem is axisymmetric, the azimuth angle does not come to the picture, and therefore, we use the axisymmetric spherical coordinates shown in the figure. The gravity is zero and the electrohydrodynamic-induced fluid shear does not lead to a net motion of the drop because of the symmetry. Therefore, the center of mass of the droplet remains at the origin of the coordinate. A uniform electric field $\mathbf{E}_0$ is imposed at the surface of the container as shown in the figure.

The physical properties of the fluids are the densities, ρ_i, ρ_o, the viscosities, μ_i, μ_o, the electric permittivities, ϵ_i, ϵ_o, and the electric conductivities, σ_i, σ_o. The surface tension is γ. The subscripts i and o denote the physical parameters inside and outside of the drop. Under the assumption of creeping flow, the governing nondimensional numbers of this problem are $\mathrm{Ca}_{el} = \mu_o u_s/\gamma$, $R = \sigma_i/\sigma_o$, $S = \epsilon_i/\epsilon_o$, $\widetilde{\mu} = \mu_i/\mu_o$, and $\lambda = a/b$. Here Ca_{el} is the electric capillary number and $u_s = \epsilon_o E_0^2 a/\mu_o$ is a velocity scale that is constructed by balance of the electric and viscous shear stresses, where $E_0 = |\mathbf{E}_0|$. Sometimes in the literature, the Ohnesorge number

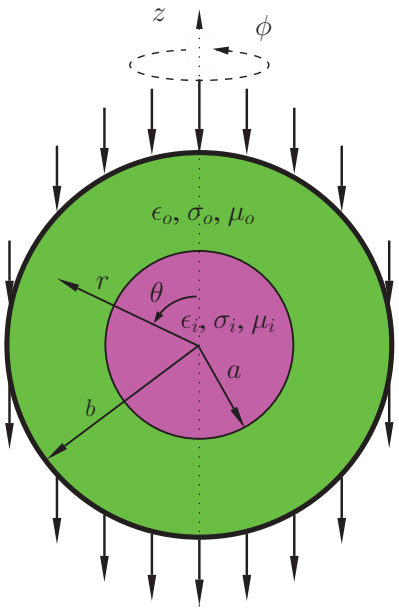

FIG. 1. (Color online) The geometric setup, depicting a liquid drop of radius a suspended in a pool of another fluid and confined by a spherical container of radius b. A uniform electric field $\mathbf{E}_0$ (V m^{-1}) is imposed at the surface of the container.

$\mathrm{Oh} = \mu_o/\sqrt{\rho_o a\gamma}$ or the nondimensional strength of the electric field $E^* = \sqrt{\mathrm{Ca}_{el}} = E_0/\sqrt{\gamma/\epsilon_o a}$ is used in lieu of Ca_{el}.

III. GOVERNING EQUATIONS

Electrohydrodynamics deals with interactions of electric field and fluid flow. As such, the laws concerning the fluid dynamics and electric field and their coupling need to be considered. Here, the governing equations are the conservations of mass and momentum, and simplified Maxwell's electromagnetic equations. For leaky dielectric fluids with constant properties and net zero charge in the bulk, it can be shown that the electric field equations are decoupled from the fluid flow equations, but the fluid flow equations are coupled to the electric field equations through the momentum jump conditions [25–27]. This decoupling allows one to solve the electric field and hydrodynamic equations sequentially.

A. Electric field equations and their solutions

The charge conservation equation, along with the fact that the electric field **E** is irrotational and divergence free, leads to the Laplace equation for the electric potential [27]:

$$\nabla^2\phi = 0. \tag{1}$$

Equation (1) is valid for fluids inside and outside of the drop and is solved using the following boundary conditions: (1) $\phi_i(0,\theta)$ should be bounded, (2) $\phi_i(a,\theta) = \phi_o(a,\theta)$, (3) $\sigma_i \partial\phi_i/\partial r(a,\theta) = \sigma_o \partial\phi_o/\partial r(a,\theta)$, and (4) $\phi_o(b,\theta) = E_0 b\cos\theta$. More details about these boundary conditions can be found in Ref. [28]. Solution of Eq. (1) yields the electric potentials for the inside

$$\phi_i = \Gamma\phi_{i_\infty}; \quad \frac{\phi_{i_\infty}}{E_0 a} = \frac{3}{R+2}\left(\frac{r}{a}\right)\cos\theta, \tag{2}$$

and the outside

$$\phi_o = \Gamma\phi_{o_\infty}; \quad \frac{\phi_{o_\infty}}{E_0 a} = \left[\left(\frac{r}{a}\right) - \frac{R-1}{R+2}\left(\frac{a}{r}\right)^2\right]\cos\theta, \tag{3}$$

where

$$\Gamma(\lambda, R) = \frac{R+2}{(R+2) - \lambda^3(R-1)} \tag{4}$$

is a correction factor that takes into account the confinement effect on the electric field. Here, ϕ_{i_∞} and ϕ_{o_∞} represent the electric potentials in an unbounded domain.

Several observations can be made about Eqs. (2)–(4). In the limit of $\lambda \to 0$, $\Gamma \to 1$, and the solution in an unbounded domain is recovered. Second, $R > 1$ results in $\Gamma > 1$ and vice versa. This suggests that for drops more (less) conducting than the ambient fluid, the confinement effect yields higher (lower) electric potential field. Third, in the two opposing limits of $R \ll 1$ and $R \gg 1$, Γ is asymptotic to $\Gamma_0 \equiv 2/(2+\lambda^3)$ and $\Gamma_\infty \equiv 1/(1-\lambda^3)$ lines, respectively. Since $\Gamma_\infty/\Gamma_0 > 1$, the confinement effect will be more pronounced for drops more conducting than the ambient fluid compared to the opposite case. Figure 2 summarizes these observation.

To understand the reason behind the variations of Γ with R and λ as depicted in Fig. 2, one needs to compare the electric potential field in the finite domain with that in an unbounded domain in the range $0 < r < b$. This comparison essentially boils down to comparing the electric potentials for the two cases at $r = 0$ and $r = b$, for a fixed θ. At $r = 0$, the electric potential is null for both cases. However, at $r = b$ the electric potential for the confined domain is $\phi(b) = E_0 b\cos\theta$, while it is $\phi_{o_\infty}(b) = E_0 b\{1 - [(R-1)/(R+2)]\lambda^3\}\cos\theta$ for the unbounded domain. It is clear that the term in the brackets is less than 1 for $R > 1$. Thus, for $R > 1$, $\phi_{o_\infty}(b) < \phi(b)$. Since the electric potential at the center of the drop is the same for both cases, therefore, the electric potential will be stronger over the range $0 < r < b$ for a bounded domain compared to an unbounded one; hence $\Gamma > 1$ for $R > 1$. A similar argument can be used to justify why $\Gamma < 1$ for $R < 1$. It should be noted that when R deviates substantially from 1, the confinement effect is stronger when $R > 1$, while it is weaker when $R < 1$. This can be verified by noting that $d\phi_{o_\infty}(b)/dR \sim 1/(R+2)^2$. Particularly, for the two extreme cases of $R \gg 1$ and $R \ll 1$, it is seen that $\phi_{o_\infty}(b) \sim E_0 b[1-\lambda^3]$ for the former, while $\phi_{o_\infty}(b) \sim E_0 b[1+(1/2)\lambda^3]$ for the latter.

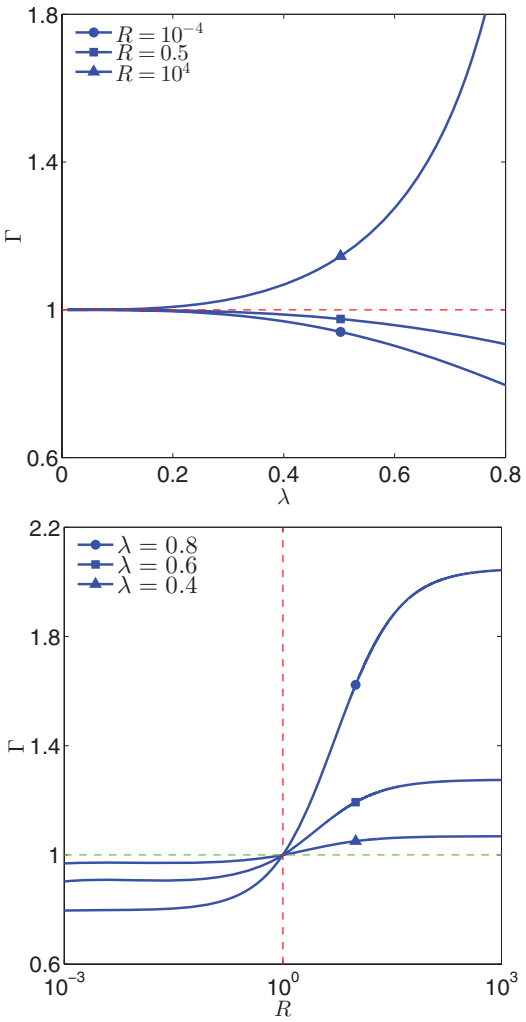

FIG. 2. (Color online) Variations of the correction factor for the electric field Γ with nondimensional domain size $\lambda = a/b$ and conductivity ratio $R = \sigma_i/\sigma_o$.

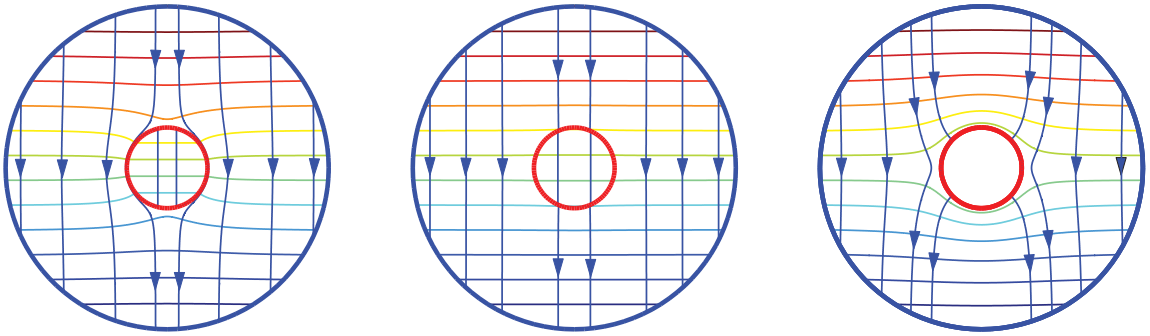

FIG. 3. (Color online) Contours of the electric potential and the electric field streamlines for fluid systems with $R = 10^{-4}$ (left panel), 0.9 (middle panel), and 10^4 (right panel) at $\lambda = 0.25$.

The electric field is found using $\mathbf{E} = -\nabla\phi$, yielding

$$\mathbf{E}_i = \Gamma\mathbf{E}_{i_\infty}; \quad \frac{\mathbf{E}_{i_\infty}}{E_0} = \frac{3}{R+2}(-\cos\theta\mathbf{e}_r + \sin\theta\mathbf{e}_\theta) \qquad (5)$$

and

$$\mathbf{E}_o = \Gamma\mathbf{E}_{o_\infty}; \quad \frac{\mathbf{E}_{o_\infty}}{E_0} = -\left[1 + \frac{2(R-1)}{R+2}\left(\frac{a}{r}\right)^3\right]\cos\theta\mathbf{e}_r + \left[1 - \frac{R-1}{R+2}\left(\frac{a}{r}\right)^3\right]\sin\theta\mathbf{e}_\theta, \qquad (6)$$

where $\mathbf{E}_{i_\infty}$ and $\mathbf{E}_{o_\infty}$ are the electric fields in an unbounded domain. To gain insight into the structure of the electric field, $\mathbf{E}_{i_\infty}$ and $\mathbf{E}_{o_\infty}$ can be rewritten in terms of the imposed electric field $\mathbf{E}_0$ [29], where it is possible to see that the electric field inside the drop is uniform and that the external electric field comprises the imposed electric field $\mathbf{E}_0$ and a field due to a dipole aligned with the field. Also, for visualization of the electric field distribution, it will be helpful to define an electric streamfunction ψ^e. This is done in a manner similar to the derivation of the velocity streamfunction ψ. Considering that $\nabla\cdot\mathbf{E} = 0$, the components of the electric field can be defined in terms of ψ^e as $E_r = [1/(r^2\sin\theta)](\partial\psi^e/\partial\theta)$ and $E_\theta = -[1/(r\sin\theta)](\partial\psi^e/\partial r)$. This yields $\psi^e_i = \Gamma\psi^e_{i_\infty}$, $\psi^e_o = \Gamma\psi^e_{o_\infty}$, where $\psi^e_{i_\infty}/E_0a^2 = -[3/(2R+4)](r/a)^2\sin^2\theta$ and $\psi^e_{o_\infty}/E_0a^2 = -(1/2)\{(r/a)^2 + [2(R-1)/(R+2)](a/r)\}\sin^2\theta$ are the electric streamfunctions in an unbounded domain. We note that the streamlines and equipotential lines are mutually orthogonal, and while the velocity streamfunction ψ is continuous at the interface, this is not the case for ψ^e as $E_{r_i}(a,\theta) \neq E_{r_o}(a,\theta)$.

The structure of the electric potential ϕ around the drop is of interest since it controls the electric stresses, which in turn control the drop deformation and fluid circulation. Inspection of Eqs. (2)–(4) shows that the electric potential is controlled by the conductivity ratio R and the confinement parameter Γ. However, the confinement parameter does not alter the structure of ϕ; rather it modifies its magnitude. Therefore, we only explore the effect of conductivity ratio R on the electric potential for a fixed domain size. Figure 3 shows the equipotential contours and streamlines (i.e., lines of forces) for three different fluid systems at $\lambda = a/b = 0.25$ and nondimensional conductivity ratios of $R = \sigma_i/\sigma_o = 10^{-4}, 0.9$, and 10^4. The first system, $R = 10^{-4}$, represents a fluid drop much less conducting than the ambient fluid, such as fluid systems C and F in Table II. The second system, $R = 0.9$, represents a drop whose electric conductivity is comparable with that of the ambient, $R \sim 1$. The third system, $R = 10^4$, represents a drop that is much more conducting than the ambient fluid, such as systems D and E in Table II. Note that the property ratios in Table II are based on the measurements of Refs. [20,30–32] as listed in Table I. For the first system, the equipotential lines inside the drop are horizontal, suggesting that the inner electric potential changes linearly in the direction of the field. Also the contour lines inside the drop are more concentrated compared with the external equipotential lines, which is an indication of the steep gradient in the drop due to its low electric conductivity. Away from the drop surface the contour lines are horizontal, but they bend toward the surface as they approach it. Here the external electric streamlines in the vicinity of the drop surface conform to the geometry by turning around as they pass the sides. This is because the normal component of the electric field $E_{n_o} \sim \partial\psi^e/\partial t$ is nearly zero

TABLE I. Physical properties of the fluids used. The surface tensions for fluid systems (1) + (2), (3) + (4), and (5) + (6) are $\gamma = 1.45\times10^{-3}, 5.5\times10^{-3}, 72.8\times10^{-3}$ N m^{-1}, respectively. Here $\epsilon_0 = 8.854\times10^{-12}$ F m^{-1} is the permittivity of the free space.

No.	Fluid	σ (S m^{-1})	ϵ (F m^{-1})	μ (Pa s)	ρ (kg m^{-3})
1	silicon oil 1	2.67×10^{-12}	$2.66\epsilon_0$	0.0167	941
2	corn oil	1.06×10^{-11}	$3.24\epsilon_0$	0.0421	914
3	silicon oil 2	3.33×10^{-11}	$2.77\epsilon_0$	12	980
4	oxidized castor oil	10^{-9}	$6.3\epsilon_0$	6.5	980
5	water	$O(10^{-4})$ to $O(10^{-2})$	$80\epsilon_0$	0.001	998.20
6	air	$O(10^{-15})$	ϵ_0	1.82×10^{-5}	1.205

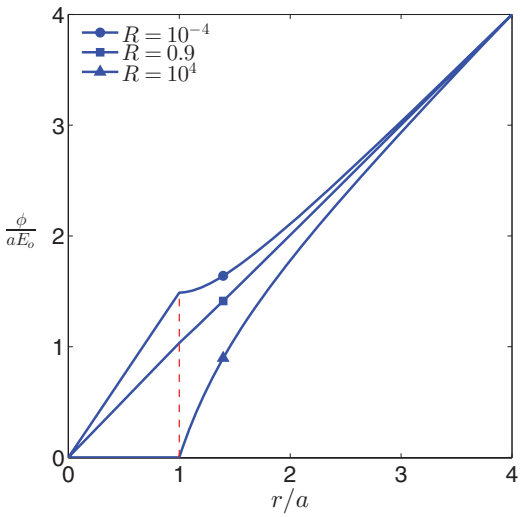

FIG. 4. (Color online) Variation of electric potential at $\theta = \pi/4$ and $\lambda = 0.25$ in the radial direction, corresponding to the fluid systems shown in Fig. 3.

at the interface, noting that $\sigma_i E_{n_i} = \sigma_o E_{n_o}$ at the interface and $\sigma_o \gg \sigma_i$. For $R = 0.9$, both equipotential lines and streamlines are nearly uniform, reflecting the fact that the electric potential field is nearly linear throughout the domain. For $R = 10^4$, the electric potential inside the drop vanishes and the drop surface becomes a surface of equipotential. Furthermore, the external equipotential lines near the interface conform to its shape by turning around as they pass the upper and the lower halves. This is because that the tangential component of electric field is nearly zero at the interface, $E_t \sim -\partial\phi/\partial t \sim 0$, which occurs because the electric field is nearly zero inside the drop ($E_{t_i} \sim 0$, $E_{n_i} \sim 0$), and the tangential component of the interfacial electric field strength is continuous, $E_{t_i} = E_{t_o}$. The streamlines, however, bend toward the interface and are normal to the interface at the intersection point as the normal gradient of the streamfunction at the interface is nearly zero; i.e., $E_t \sim \partial\psi^e/\partial n \sim 0$. Figure 4, which shows the variation of $\phi(r,\pi/4)$ in the radial direction, summarizes some of these observations.

1. The electric surface charge

The strength and distribution of the free charges have a profound effect on the sense of drop deformation and fluid circulation. The charge density (C m^{-2}) can be found from $q_s = [\![\epsilon \mathbf{E}]\!] \cdot \mathbf{n}$, where $\mathbf{n}$ is an outward unit vector normal to the interface [27]. Here the symbol $[\![\,]\!]$ denotes the jump in a physical parameter, such as a Q, at the interface:

$$[\![Q]\!] = Q_o - Q_i. \tag{7}$$

Considering the continuity of electric current density at the interface ($\sigma_i E_{n_i} = \sigma_o E_{n_o}$) yields $q_s = \epsilon_o E_{n_o}(1 - S/R)$, E_n being the normal component of $\mathbf{E}$. Evaluation of $E_{n_o} \equiv E_{r_o}$ at the interface from Eq. (6) and substitution of the resulting expression into the statement for q_s leads to

$$q_s = \Gamma q_{s_\infty}; \quad \frac{q_{s_\infty}}{\epsilon_o E_0} = \frac{3(S-R)}{R+2}\cos\theta, \tag{8}$$

where q_{s_∞} is the free surface charge density in an unbounded domain.

2. The jump in electrical stresses

The interfacial jumps in the tangential and normal electric stresses are the drivers behind the fluid flow circulation and interface deformation, respectively. To calculate these terms, the electric stresses must be evaluated first using the Maxwell stress tensor

$$\boldsymbol{\tau}^e = \epsilon \mathbf{E}\mathbf{E} - \tfrac{1}{2}E^2\epsilon\mathbf{I}, \tag{9}$$

where $E^2 = \mathbf{E}\cdot\mathbf{E}$ and $\mathbf{I}$ is the identity tensor. Here it is more useful to express these stresses in terms of a tangent-normal coordinate system and to customize the resulting expressions for other coordinates afterward. Doing so, the stresses will be valid for a general interface in any coordinate system. In a t-n coordinate system, $\mathbf{E} = E_t\mathbf{t} + E_n\mathbf{n}$, where $E_t = -\partial\phi/\partial t$, $E_n = -\partial\phi/\partial n$, $\mathbf{t}$ is a unit vector tangent to the drop in the counterclockwise direction, and $\mathbf{n}$ is a unit vector normal to the drop in the outward direction. Accordingly, the jumps in the normal and tangential electric stresses are

$$[\![\tau^e_{nn}]\!] = \frac{\epsilon_o}{2}\left[\left(1 - \frac{S}{R^2}\right)E^2_{n_o} + (S-1)E^2_t\right] \tag{10}$$

and

$$[\![\tau^e_{nt}]\!] = \epsilon_o E_{n_o} E_t \left(1 - \frac{S}{R}\right) = q_s E_t, \tag{11}$$

respectively. For the problem at hand where $E_n \equiv E_r$ and $E_t \equiv E_\theta$, evaluation of E_r and E_θ at the interface using Eqs. (5) and (6) and substitution of the resulting expressions into Eq. (10) yields

$$\begin{aligned} [\![\tau^e_{rr}]\!] &= \Gamma^2 [\![\tau^e_{rr}]\!]_\infty; \\ \frac{[\![\tau^e_{rr}]\!]_\infty}{\epsilon_o E_0^2} &= \frac{9}{2}\frac{(R^2+1-2S)\cos^2\theta + S - 1}{(R+2)^2}, \end{aligned} \tag{12}$$

where $[\![\tau^e_{rr}]\!]_\infty$ is the jump in the normal stress in an unbounded domain. Similarly, the jump in the tangential electric stress is found:

$$[\![\tau^e_{r\theta}]\!] = \Gamma^2 [\![\tau^e_{r\theta}]\!]_\infty; \quad \frac{[\![\tau^e_{r\theta}]\!]_\infty}{\epsilon_o E_0^2} = \frac{9}{2}\frac{S-R}{(R+2)^2}\sin 2\theta, \tag{13}$$

where $[\![\tau^e_{r\theta}]\!]_\infty$ is the jump in the tangential stress in an unbounded domain.

In summary, the confinement leads to rescaling of ϕ_∞, ψ^e_∞, $\mathbf{E}_\infty$, and q_{s_∞} by Γ, and rescaling of $[\![\tau^e_{rr}]\!]_\infty$ and $[\![\tau^e_{r\theta}]\!]_\infty$ by Γ^2. However, it does not alter the structure of any of these entities.

B. Fluid flow equations and their solutions

The governing equations for steady-state, incompressible, and creeping flows are the conservations of mass $\nabla\cdot\mathbf{u} = 0$ and momentum $-\nabla p + \mu\nabla^2\mathbf{u} + \mathbf{F}^e = 0$, where $\mathbf{u}$ is the fluid velocity, p is the pressure, and $\mathbf{F}^e = \nabla\cdot\boldsymbol{\tau}^e = q_v\mathbf{E} - (1/2)E^2\nabla\epsilon$ is the electric force density. Here $q_v = \nabla\cdot\epsilon\mathbf{E}$ is the volumetric free charge density (C m^{-3}). For leaky dielectric fluids with constant properties, $\mathbf{F}^e$ is zero in the fluid bulk, since $q_v = 0$ and $\nabla\epsilon = 0$. As such, the electric force enters the picture only through the momentum jump conditions. Here it is possible to derive an equation for the streamfunction ψ, which satisfies

the mass and momentum conservation equations

$$D^4\psi = 0, \tag{14}$$

where $D^4 = D^2(D^2)$, D^2 being the well-known operator that resembles Laplacian. Equation (14) is valid for fluids inside and outside of the drop and is solved using the following boundary conditions: (1) u_{r_i} and u_{θ_i} should be bounded at $r = 0$, (2) $u_{\theta_i}(a,\theta) = u_{\theta_o}(a,\theta)$, (3) $u_{r_i}(a,\theta) = u_{r_o}(a,\theta) = 0$, (4)$[\![\tau^h_{r\theta}]\!] + [\![\tau^e_{r\theta}]\!] = 0$, where $\tau^h_{r\theta}$ is the hydrodynamic shear stress, (5) $u_{r_o}(b,\theta) = u_{\theta_o}(b,\theta) = 0$. Boundary condition (4) suggests a solution of the form $\psi(r,\theta) = r^n \sin^2\theta\cos\theta$, where n is a real constant to be determined. Substitution for $\psi = r^n \sin^2\theta\cos\theta$ into Eq. (14) results in an algebraic equation for n, the solution of which leads to $n = 0$, -2, 3, and 5. Accordingly, $\psi_o = (A + Br^{-2} + Cr^3 + Dr^5)\sin^2\theta\cos\theta$ and $\psi_i = (E + Fr^{-2} + Gr^3 + Hr^5)\sin^2\theta\cos\theta$, where A–H are constants to be determined. Application of boundary condition (1) results in $E = F = 0$, and application of the rest of the boundary conditions yields $A = U_{\max}a^2\Lambda_A/\Lambda_E$, $B = U_{\max}a^4\Lambda_B/\Lambda_E$, $C = U_{\max}a^{-1}\Lambda_C/\Lambda_E$, $D = U_{\max}a^{-3}\Lambda_D/\Lambda_E$, $G = U_{\max}a^{-1}$, and $H = -U_{\max}a^{-3}$, where $U_{\max}$ is the maximum velocity at the surface of the drop and Λ_A–Λ_E are coefficients that are functions of λ (Appendix A). Accordingly, the streamfunctions for the fluids inside and outside are

$$\frac{\psi_i}{U_{\max}a^2} = \left[\left(\frac{r}{a}\right)^3 - \left(\frac{r}{a}\right)^5\right]\sin^2\theta\cos\theta \tag{15}$$

and

$$\frac{\psi_o}{U_{\max}a^2} = \frac{1}{\Lambda_E}\left[\Lambda_B\left(\frac{a}{r}\right)^2 + \Lambda_A + \Lambda_C\left(\frac{r}{a}\right)^3 + \Lambda_D\left(\frac{r}{a}\right)^5\right]\sin^2\theta\cos\theta, \tag{16}$$

and the velocities are

$$\frac{u_{r_i}}{U_{\max}} = \left[\left(\frac{r}{a}\right)^3 - \left(\frac{r}{a}\right)\right](1 - 3\cos^2\theta), \tag{17}$$

$$\frac{u_{\theta_i}}{U_{\max}} = \frac{1}{2}\left[5\left(\frac{r}{a}\right)^3 - 3\left(\frac{r}{a}\right)\right]\sin 2\theta, \tag{18}$$

$$\frac{u_{r_o}}{U_{\max}} = -\frac{1}{\Lambda_E}\left[\Lambda_B\left(\frac{a}{r}\right)^4 + \Lambda_A\left(\frac{a}{r}\right)^2 + \Lambda_C\left(\frac{r}{a}\right) + \Lambda_D\left(\frac{r}{a}\right)^3\right](1 - 3\cos^2\theta), \tag{19}$$

and

$$\frac{u_{\theta_o}}{U_{\max}} = \frac{1}{2\Lambda_E}\left[2\Lambda_B\left(\frac{a}{r}\right)^4 - 3\Lambda_C\left(\frac{r}{a}\right) - 5\Lambda_D\left(\frac{r}{a}\right)^3\right]\sin 2\theta. \tag{20}$$

The maximum surface velocity is

$$U_{\max} = \Omega U_{\max_\infty}; \quad U_{\max_\infty} = \frac{9}{10}\frac{u_s}{1+\widetilde{\mu}}\frac{S-R}{(R+2)^2}, \tag{21}$$

where $U_{\max_\infty}$ is the maximum surface velocity in an unbounded domain, $u_s = \epsilon_o E_0^2 a/\mu_o$ is the velocity scale, and

$$\Omega(\lambda, R, \widetilde{\mu}) = \Gamma^2\frac{\Lambda_E(1+\widetilde{\mu})}{\widetilde{\mu}\Lambda_E + \Lambda_B + \Lambda_D} \tag{22}$$

is a correction factor that accounts for the confinement effect on the velocity field.

A few observations can be made about Eqs. (15)–(22). First, in the limit of $\lambda \to 0$, the solution in an unbounded domain is recovered. Second, the streamfunctions ψ_i and ψ_o are zero along the lines $\theta = 0$, $\theta = \pi/2$, $\theta = \pi$, and the surfaces of the drop $r = a$ and the container $r = b$. These lines are the dividing streamlines, which divide the flow field to eight quadrants. Third, evaluation of Eqs. (18) and (20) at $r = a$ shows that $u_{\theta_i}(a,\theta) = u_{\theta_o}(a,\theta) = U_{\max}\sin 2\theta$, and therefore the maximum surface velocity takes place at angles $\theta = \pi/4$ and $\theta = 3\pi/4$. Fourth, the flow strength is characterized by $U_{\max}$, as formulated by Eqs. (21) and (22). For a given fluid system, the confinement affects the maximum surface velocity $U_{\max}$ through Ω. The sign of Ω is always positive, and therefore the sense of flow circulation is controlled by the sign of $U_{\max}$, which in turn is determined by the relative magnitudes of R and S. For $R < S$, $U_{\max} > 0$, and vice versa. Therefore, for $R < S$ the ambient fluid flows from the poles toward the equator, while for $R > S$ the direction of the flow is reversed. The sense of flow circulation correlates positively with the sense of the net shear stress, given by Eq. (13). Fifth, comparison of Eqs. (15) with (B1) and (16) with (B2) shows that the confinement affects the structure of the outer flow field, but it does not alter the the structure of the inner one.

To explore the confinement effect on the velocity field, in Fig. 5 we plot nondimensional streamlines for a fluid system with $R < S$ at three different nondimensional domain sizes of $\lambda = a/b = 0.5$, 0.25, and 0. This fluid system represents, for example, systems A, C, and F of Table II. Here $U_{\max} > 0$, and therefore, the ambient fluid runs from the poles toward the equator. The flow consists of four toroidal vortices inside the drop that are matched with their counterparts in the ambient fluid. The streamlines in the ambient fluid are initially in the form of closed curves. However, as the domain size increases, the closed curves expand and eventually transform to open curves. The open circles mark the positions of the cores of the inner vortices. The fluid flow decays away from the drop as is evidenced from the divergence of the streamlines. Furthermore, the velocity field is weaker in the poles compared with that in the equator. As the domain size increases, the cores of the external vortices move gradually outward, while the cores of the inner vortices remain stationary. The r and θ coordinates of the inner cores can be found by setting u_{θ_i} and u_{r_i} to zero, respectively, leading to $r = \sqrt{3/5}a$ and $\theta_1 = \cos^{-1}(1/\sqrt{3}) \simeq 55^\circ$ and $\theta_2 = \cos^{-1}(-1/\sqrt{3}) \simeq 145^\circ$. The fact that $\theta_1 > \pi/4$ and $\theta_2 > 3\pi/4$ suggests that the flow is stronger near the equator. For fluid systems B, D, E where $R > S$, the flow structure will be exactly the same but the sense of flow circulation will be the opposite.

Figure 6 shows the variation of nondimensional radial and tangential velocities versus r/a for the flow fields shown in Fig. 5. Here the radial velocity u_r is plotted at $\theta = 0$, where it is maximum in an absolute sense, and the tangential velocity u_θ is plotted at $\theta = \theta_1 \simeq 55^\circ$ to show the effect of confinement on the evolution of the radial coordinate of the cores of the external vortices. For both bounded and unbounded domains, the radial velocity is zero at the center $r = 0$ and the drop surface $r = a$, while it reaches a maximum at $r/a = \sqrt{3}/3$. For the unbounded domain, the outer radial velocity u_{r_o} reaches a local

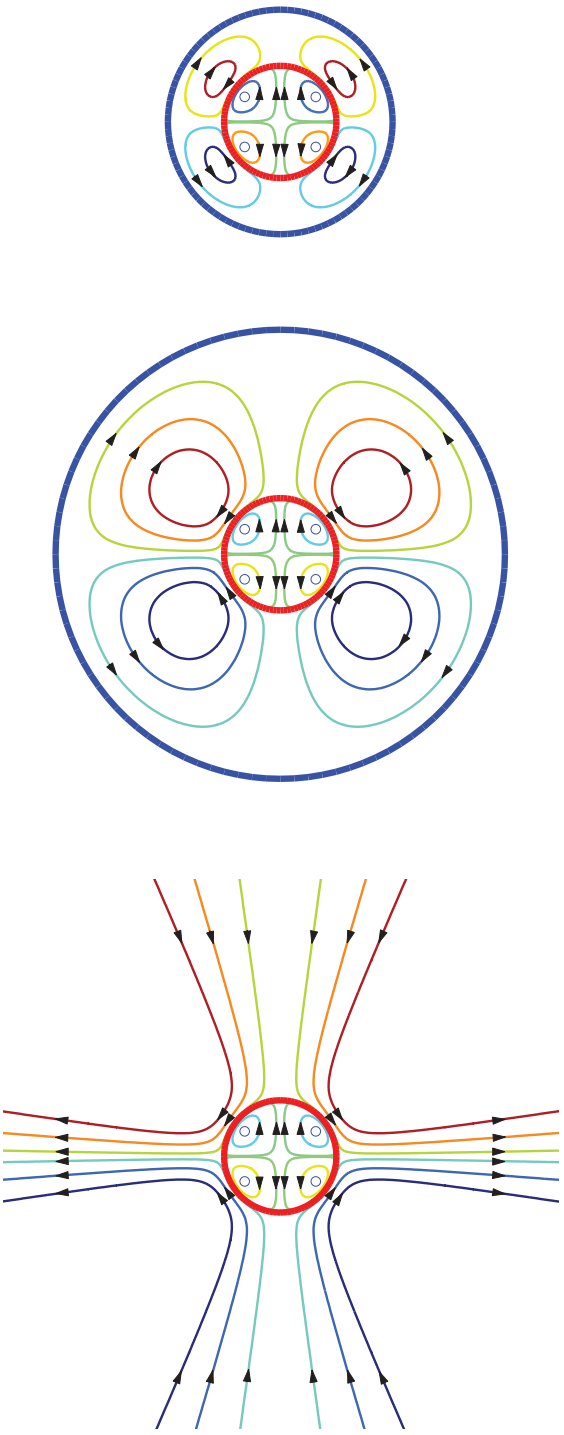

FIG. 5. (Color online) Nondimensional streamlines for a fluid system with $R < S$ at $\lambda = 0.5$ (top panel), 0.25 (middle panel), and 0 (bottom panel). Here the ambient fluid runs from the poles toward the equator.

maximum in an absolute sense in $r/a = \sqrt{2}$ and gradually decays until it levels off to zero. As the domain size becomes smaller, the magnitude of the local maximum of u_{r_o} becomes smaller and also the velocity decays faster. The tangential velocity is zero at the center and at the cores of the internal and external vortices. It gradually decays away from the surface for the unbounded domain, while it abruptly drops off to zero at $r = b$ for the bounded domains. Comparing the radial and the tangential velocities at a fixed λ, it is seen that the rate of decay of the tangential velocity is faster. In particular, for the unbounded domain, $u_{\theta_o} \sim 1/(r/a)^4$, while $u_{r_o} \sim 1/(r/a)^2$.

The effect of confinement on the strength of the flow field is characterized by $\Omega(\lambda, R, \widetilde{\mu})$, according to Eqs. (21) and (22). The fact that Ω depends on both R and $\widetilde{\mu}$ indicates that the confinement affects the flow field through both the electric and hydrodynamic forces. To isolate these effects, we decompose Ω to two parts by rewriting it as $\Omega = \Omega^e \Omega^h$, where $\Omega^e = \Gamma^2$ and $\Omega^h = [\Lambda_E(1+\widetilde{\mu})]/[\widetilde{\mu}\Lambda_E + \Lambda_B + \Lambda_D]$ are two subfactors that represent the electric and hydrodynamic effects, respectively. Figure 7 shows the variations of Ω, Ω^e, and Ω^h with λ. As is evident, Ω is (essentially) a monotonic function of λ, and except for fluid systems B, D, and E, it is a decreasing function of λ. The behavior of $\lambda - \Omega^e \equiv \Gamma^2$ curve is similar to that of $\lambda - \Gamma$ curve, described in Fig. 2, i.e., $\Omega^e \equiv \Gamma^2$ increases with λ for systems with $R > 1$ and vice versa. The λ-Ω^h curve, however, is monotonically decreasing with λ for all the systems, but the rate of decay is inversely proportional to $\widetilde{\mu}$. The behavior of Ω, however, depends on the interplay of Ω^e and Ω^h, resulting in an increase in $U_{\max}$ for systems E, a decrease for systems A, C, and F, and essentially no changes for systems B and D.

IV. DROP DEFORMATION

The analysis so far was based on the premise that the drop remains spherical. However, the drop is likely to deform as a result of the electric and hydrodynamic stresses. For small deformation, it is possible to calculate the distortion from spherical shape using normal stress balance at the drop surface

$$[\![\tau^e_{rr}]\!] + [\![\sigma^h_{rr}]\!] = \gamma\kappa, \tag{23}$$

where $[\![\sigma^h_{rr}]\!] = [\![\tau^h_{rr}]\!] - [\![p]\!]$ is the jump in the total normal hydrodynamic stress ($[\![\tau^h_{rr}]\!]$ is the jump in the the deviatoric part and $[\![p]\!]$ is the jump in the pressure), γ is the surface tension, and κ is twice the mean curvature of the drop. The form of the jump in the normal electric stresses, Eq. (12), suggests that the drop shape function ξ should be of the form

$$\xi = a[1 + (2\mathcal{D}/3)(3\cos^2\theta - 1)]. \tag{24}$$

Here $\mathcal{D} = (z_{\max} - r_{\max})/(z_{\max} + r_{\max})$ is the Taylor deformation parameter [12], which needs to be determined, $z_{\max}$ and $r_{\max}$ being the end-to-end length of the drop in the direction of electric field and the maximum breadth in the traverse direction, respectively. We note that Eq. (24) and its variants have been used by others, including Ref. [15], and that this equation satisfies the incompressibility condition. Here, we assume that the drop deformation $\mathcal{D}$ is small (i.e., $\mathrm{Ca}_{el} \ll 1$); therefore the interfacial jump conditions are imposed at $r = a$ rather than $r = \xi$. This assumption implies that the r-θ coordinate system is a tangent-normal coordinate system. The detailed justification for this assumption can be found in Ref. [33]. The components of Eq. (23) are computed as follows. The net normal electric stress $[\![\tau^e_{rr}]\!]$ is already available from Eq. (12), and for small deformation

$$\kappa = \frac{2}{a} + \frac{8\mathcal{D}(3\cos^2\theta - 1)}{3a}, \tag{25}$$

TABLE II. Ratios of the material properties (i.e., drop property over that of the ambient) for selected fluid systems. The individual properties are as listed in Table I.

System	Fluids	R	S	$\widetilde{\mu}$	$\widetilde{\rho}$
A	silicon oil 1 in corn oil	0.252	0.820	0.3975	1.03
B	corn oil in silicon oil 1	3.97	1.22	2.515	0.97
C	silicon oil 2 in oxidized castor oil	0.033	0.4397	1.8462	1
D	oxidized castor oil in silicon oil 2	30.03	2.274	0.5417	1
E	water in air	$O(10^{11})$ to $O(10^{13})$	80	54.95	828.38
F	air in water	$O(10^{-11})$ to $O(10^{-13})$	0.0125	0.0182	0.001

according to Ref. [33]. To compute $[\![\sigma^h_{rr}]\!]$, $[\![\tau^h_{rr}]\!]$ is found from the velocity field, leading to

$$[\![\tau^h_{rr}]\!] = \Omega [\![\tau^h_{rr}]\!]_\infty; \quad \frac{[\![\tau^h_{rr}]\!]_\infty}{\mu_o U_{\max_\infty}/a} = 4(1-\widetilde{\mu})(1-3\cos^2\theta), \tag{26}$$

where $[\![\tau^h_{rr}]\!]_\infty$ is the jump in the deviatoric normal hydrodynamic stress in an unbounded domain. The pressure jump is found by integration of the momentum equation, $-\boldsymbol{\nabla} p + \mu \nabla^2 \mathbf{u} = 0$, leading to

$$\frac{[\![p]\!]}{\mu_o U_{\max}/a} = \left[2 - 7\widetilde{\mu} + \frac{5\Lambda_C}{\Lambda_E}\right](1-3\cos^2\theta), \tag{27}$$

where we have ignored the constants of integration as they will be balanced with the other isotropic terms of Eq. (23). Thus, the jump in the total normal hydrodynamic stress is

$$\frac{[\![\sigma^h_{rr}]\!]}{\mu_o U_{\max_\infty}/a} = \Gamma^2 \mathcal{F}(1+\widetilde{\mu})(1-3\cos^2\theta), \tag{28}$$

where

$$\mathcal{F}(\lambda,\widetilde{\mu}) = \frac{(2+3\widetilde{\mu})\,\Lambda_E - 5\Lambda_C}{\widetilde{\mu}\Lambda_E + \Lambda_B + \Lambda_D} \tag{29}$$

is a characteristic function that, in conjunction with $U_{\max_\infty}$, determines the sense of $[\![\sigma^h_{rr}]\!]$. Figure 8 shows the variations of $\mathcal{F}$ with $\lambda = a/b$ for the fluid systems of Table II. As is evident, $\mathcal{F}$ decreases monotonically with λ but the rate of decay is inversely proportional to $\widetilde{\mu}$, which is in line with the behavior of Ω^h seen in Fig. 7.

Substituting for $[\![\tau^e_{rr}]\!]$, $[\![\sigma^h_{rr}]\!]$, and κ from Eqs. (12), (28), and (25), respectively, into Eq. (23) and equating the coefficients of $\cos^2\theta$ in both sides of the resulting expression yield the drop deformation

$$\mathcal{D} = \frac{9\mathrm{Ca}_{el}}{16}\frac{\Gamma^2\Phi}{(R+2)^2}, \tag{30}$$

where

$$\Phi = R^2 + 1 - 2S + \tfrac{3}{5}\mathcal{F}(R-S) \tag{31}$$

is the characteristic function that determines the shape of the drop. In the limit of $\lambda \to 0$, $\mathcal{F}(\lambda,\widetilde{\mu}) = (3\widetilde{\mu}+2)/(\widetilde{\mu}+1) \equiv \mathcal{F}_\infty$, $\Gamma^2 = 1$, and the deformation of a drop in an unbounded domain [15] is recovered:

$$\mathcal{D}_\infty = \frac{9\mathrm{Ca}_{el}}{16}\frac{\Phi_\infty}{(R+2)^2}, \tag{32}$$

where

$$\Phi_\infty = R^2 + 1 - 2S + \frac{3}{5}\frac{3\widetilde{\mu}+2}{\widetilde{\mu}+1}(R-S). \tag{33}$$

As is evident from Eq. (30), the sense of drop deformation depends on the sign of Φ; for $\Phi > 0$, $\mathcal{D} > 0$, and the drop will deform to a prolate ellipsoid; for $\Phi < 0$, $\mathcal{D} < 0$, and the drop will deform to an oblate ellipsoid; and for $\Phi = 0$, $\mathcal{D} = 0$, and the drop retains its spherical shape, despite the action of the electric forces. The domain confinement rescales

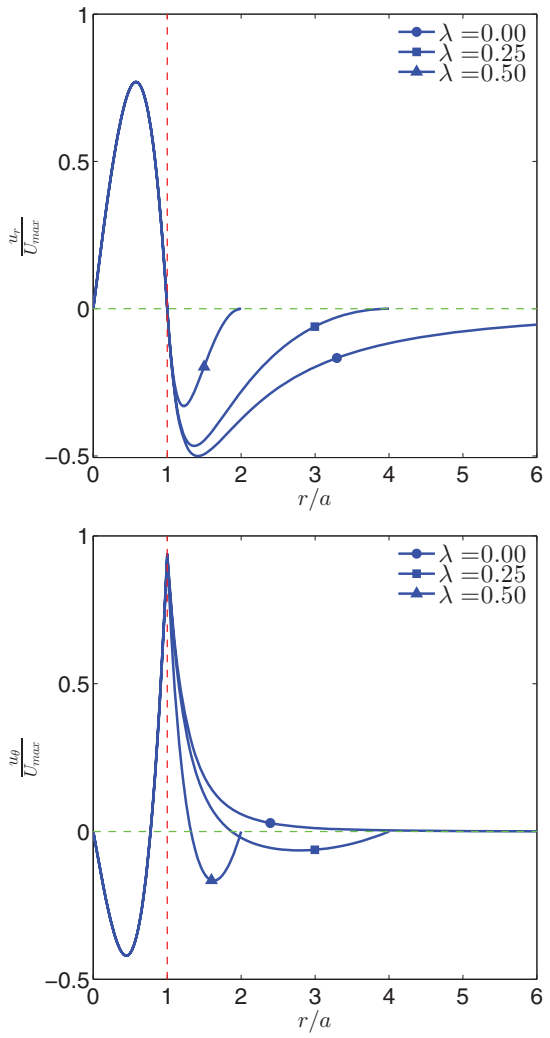

FIG. 6. (Color online) Variations of the radial $u_r/U_{\max}$ and tangential velocity $u_\theta/U_{\max}$ with r/a for the flow fields of Fig. 5. Here u_r is evaluated at $\theta = 0$, while u_θ is evaluated at $\theta = \theta_1 \simeq 55^\circ$.

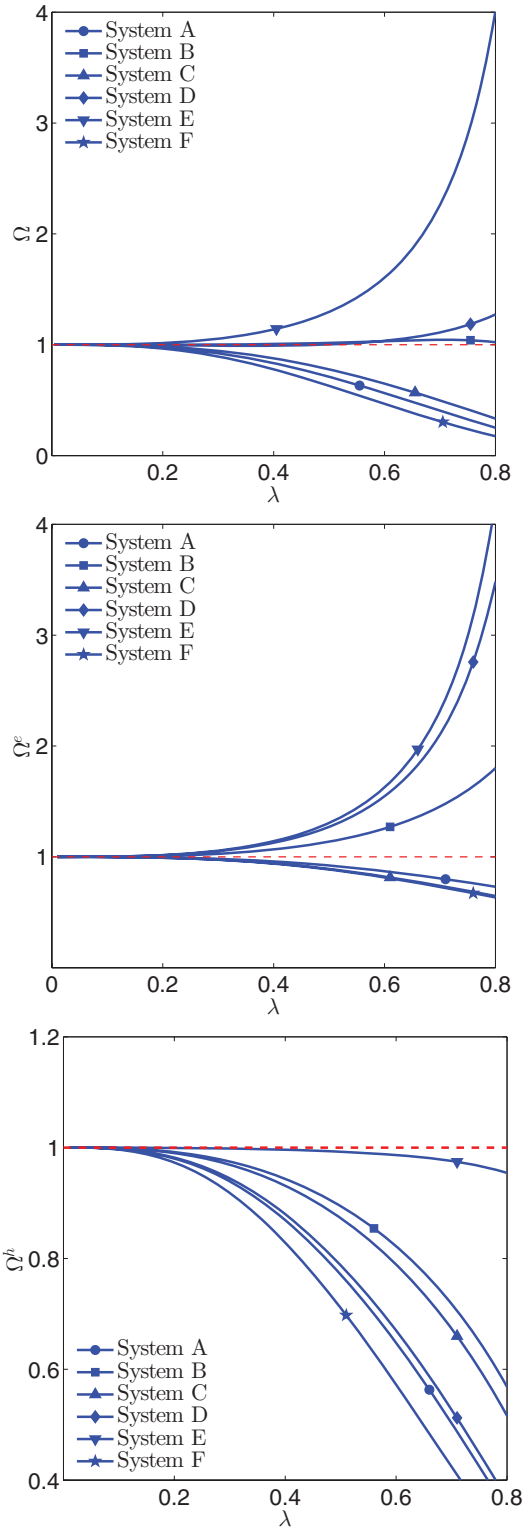

FIG. 7. (Color online) Variations of the correction factor for the strength of the velocity field Ω (top panel), a correction subfactor accounting for the electric effect Ω^e (middle panel), and a correction subfactor accounting for the hydrodynamic effect Ω^h (bottom panel) with λ.

the magnitude of the deformation parameter $\mathcal{D}_\infty$ by Γ^2, and modifies its formulation by modification of Φ_∞. We note

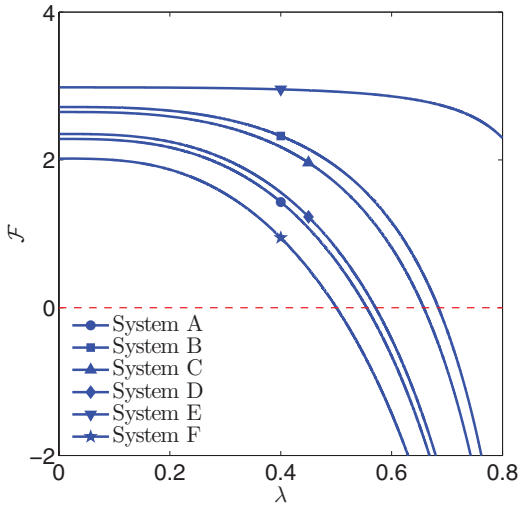

FIG. 8. (Color online) Variation of the characteristic function $\mathcal{F}$ with the nondimensional domain size λ for the fluid systems of Table II.

that $\mathrm{Ca}_{el} \sim E_0^2$, and therefore the deformation parameter $\mathcal{D}$ scales with E_0^2, a fact that has been verified by several authors for a drop in an unbounded domain; see, for example, Refs. [15,17,18]).

Figure 9 shows the variations of the nondimensional deformation parameter $\mathcal{D}/|\mathcal{D}_\infty|$ with λ for the fluid systems listed in Table II. Other pertinent information about these cases can be found in Table III. For sufficiently large domains (i.e., $\lambda \lessapprox 0.2$) the deformation is essentially independent of the domain size. However, beyond $\lambda \sim 0.2$ the confinement effect becomes visible. Three different behaviors can be detected for these fluid systems: (1) the drops in systems *A* and *C*, which are initially oblate, become less and less deformed and eventually turn into a prolate, (2) the deformations of the drops in systems *D* and *E*, which are initially prolate, increase, and (3) the deformations of the drops in systems *B* and *F*, which are

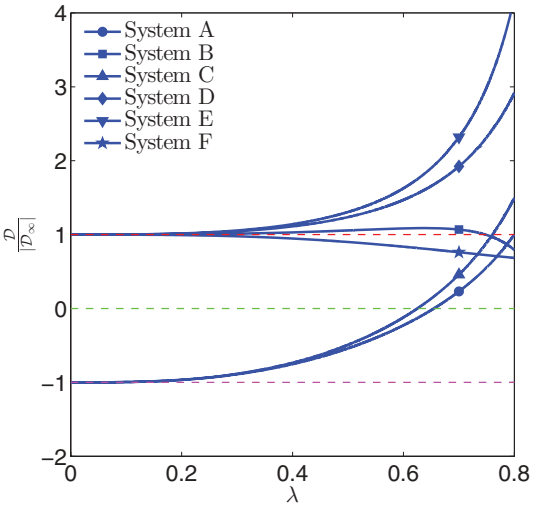

FIG. 9. (Color online) Variation of the deformation parameter $\mathcal{D} = (z_{\max} - r_{\max})/(z_{\max} + r_{\max})$ with nondimensional domain size $\lambda = a/b$ for the fluid systems of Table II. Other pertinent information is given in Table III.

TABLE III. The pertinent information about Fig. 9.

System	a (m)	E_0 (V m^{-1})	Ca$_{el}$	Oh
A	0.001	5000	4.95×10^{-4}	1.156
B	0.001	5000	4.06×10^{-4}	0.4521
C	0.001	5000	2.54×10^{-4}	88.54
D	0.001	5000	1.11×10^{-4}	163.451
E	0.001	10	1.22×10^{-11}	0.0019
F	0.001	1000	9.73×10^{-6}	0.0037

initially prolate, does not change significantly. The observed behavior is due to two reasons: (1) change in magnitude of both $[\![\tau^e_{rr}]\!]$ and $[\![\sigma^h_{rr}]\!]$ due to change in Γ^2, and (2) the change in magnitude and the sign of $[\![\sigma^h_{rr}]\!]$ due to change in $\mathcal{F}$. This will be discussed in more detail in Sec. V.

V. DEFORMATION-CIRCULATION MAP

The possible senses of drop deformation and fluid circulation around the drop can be presented in a so-called deformation-circulation map in S-R coordinates. For an unbounded domain, the map not only represents the steady-state dynamics of an isolated drop but also provides useful information about the modes of interactions of two drops at finite distances. See, for example, Refs. [20,24,28,29]. To construct this map, we note that the $\Phi = 0$ curve divides the S-R domain into two regions of oblate ($\Phi < 0$) and prolate deformation ($\Phi > 0$). We further note that the $R = S$ line delineates the domain into two parts according to the sense of fluid flow around the drop; for $R < S$ the flow will be from the poles to the equator while for $R > S$ the flow will be in the opposite direction. When the $\Phi = 0$ curve and $R = S$ line are plotted together, it results in a map of the expected shape (oblate/prolate) and fluid circulation (poles to equator/equator to poles). Figure 10 shows the deformation-circulation map and the corresponding regions, identified as regions O, $P1$, and $P2$, for a drop in an unbounded domain. Notice that since Φ is a weak function of $\widetilde{\mu}$, $\Phi = 0$ is plotted only for $\widetilde{\mu} = 1$.

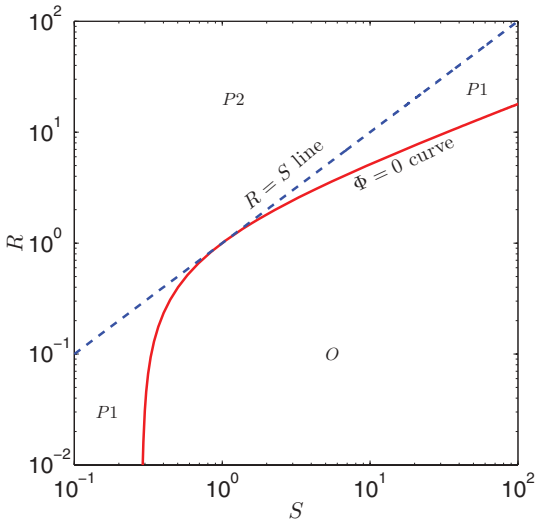

FIG. 10. (Color online) Deformation-circulation map for a drop in an unbounded domain.

In region O, $\Phi < 0$ and $R < S$, the drop deforms to an oblate ($\mathcal{D} < 0$) and the flow is from the poles to the equator. In region $P1$, $\Phi > 0$ and $R < S$, the drop becomes prolate ($\mathcal{D} > 0$) and the flow is from the poles to the equator. In region $P2$, $\Phi > 0$ and $R > S$, the drop becomes prolate ($\mathcal{D} > 0$) and the flow is from the equator to the poles. Accordingly, pole-to-equator flow ($R < S$) is the necessary condition for drop to become oblate or to retain its spherical shape.

To find out how the confinement affects the sense of drop deformation and fluid circulation, we follow the evolution of the zero-deformation curve with $\lambda = a/b$ in the deformation-circulation map. For a fixed λ, setting $\Phi = 0$ results in a quadratic algebraic equation in terms of R, $\Phi \equiv \mathcal{A}R^2 + \mathcal{B}R + \mathcal{C}(S) = 0$, where $\mathcal{A} = 1$, $\mathcal{B} = (3/5)\mathcal{F}$, and $\mathcal{C}(S) = 1 - S[(3/5)\mathcal{F} + 2]$. Assigning discrete values to S in the range $0.1 < S < 100$, the roots of the algebraic equation give the corresponding values of R that make $\Phi = 0$; i.e., $R_{1,2} = (1/2)[-(3/5)\mathcal{F} \pm \sqrt{\Delta}]$, where $\Delta = \mathcal{B}^2 - 4\mathcal{A}\mathcal{C}$ is the discriminant. Inspection of the quadratic algebraic equation and its roots shows that the possible solutions can be identified based on the three parameters $S_\mathcal{C}$, S_Δ, and $\mathcal{F}_{cr}$. Here $S_\mathcal{C} \equiv 1/[2 + (3/5)\mathcal{F}]$ and $S_\Delta \equiv [2 - (3/5)\mathcal{F}]/4$ are the two points along the S axis where $\mathcal{C}(S_\mathcal{C}) = 0$ and $\Delta = 0$, respectively, and $\mathcal{F}_{cr} = -10/3$ is the $\mathcal{F}$ where $S_\mathcal{C} \to \infty$ and $\Delta = 0$. We note that $S_\mathcal{C}/S_\Delta = 4/[4 - (9/25)\mathcal{F}^2]$, and therefore, $S_\mathcal{C}$ is always greater than S_Δ. Three possibilities exist, depending on the sign of $\mathcal{F}$ and its magnitude relative to $\mathcal{F}_{cr}$. For $\mathcal{F} > 0$, there is one solution for $S > S_\mathcal{C}$. For $\mathcal{F}_{cr} < \mathcal{F} < 0$, there are two solutions for $S_\Delta < S < S_\mathcal{C}$ and one solution for $S > S_\mathcal{C}$. For $\mathcal{F} < \mathcal{F}_{cr}$, there are two solutions for $S < S_\Delta$. It is interesting to note that for $\mathcal{F} = \mathcal{F}_{cr}$, the zero-deformation curve transforms to the $R = 1$ line, according to Eqs. (29) and (31).

Figure 11 shows the deformation-circulation map at selected values of $\lambda = a/b$. Here the viscosity ratio is $\widetilde{\mu} = 0.3975$ and $\mathcal{F}_\infty = 2.2844$. In this figure, O, $P1$, and $P2$ denote oblate, prolate 1, and prolate 2, as in Fig. 10. For panels (a) and (b), $\mathcal{F} > 0$ and the map is very similar to that for a drop in an unbounded domain. For these two panels, S_Δ does not play a role since it falls in the no-solution region ($S < S_\mathcal{C}$). For panels (c)–(f), $\mathcal{F}_{cr} < \mathcal{F} < 0$ and there are two solutions for $S_\Delta < S < S_\mathcal{C}$ and one solution fo $S > S_\mathcal{C}$. Note that for panel (f), $S_\mathcal{C} = 500$. Panel (f) marks a new development in the solution. Here $\mathcal{F}$ is essentially the same as $\mathcal{F}_{cr}$. Consequently, a slight decrease in the domain size results in $\mathcal{F} = -3.37 \lessapprox \mathcal{F}_{cr}$, and therefore shifting of the $\Phi = 0$ curve from $S > S_\Delta$ region to $S < S_\Delta$ region [panel (g)]. From this point onward, $S_\mathcal{C}$ does not play a role since it is negative and will remain so. The interesting outcome of decreasing $\mathcal{F}$ below $\mathcal{F}_{cr}$ is that the necessary condition for having an oblate deformation is now $R > S$, which is the opposite to that for a drop in an unbounded domain, and also opposite to that for a drop in a bounded domain when $\lambda < \lambda_{cr}$, λ_{cr} being the domain size that leads to $\mathcal{F} = -10/3 \equiv \mathcal{F}_{cr}$. For panels (g)–(i), there are two solutions for $S < S_\Delta$ and the size of the oblate region gradually increases.

The physical interpretation of the results shown in Figs. 9 and 11 is described in the present and the next paragraph. The sense of drop deformation is set by the net normal electric and hydrodynamic stresses, $[\![\tau^e_{rr}]\!]$ and $[\![\sigma^e_{rr}]\!]$, according to Eq. (23). The individual contribution of these stresses in the deformation can be quantified by inspection

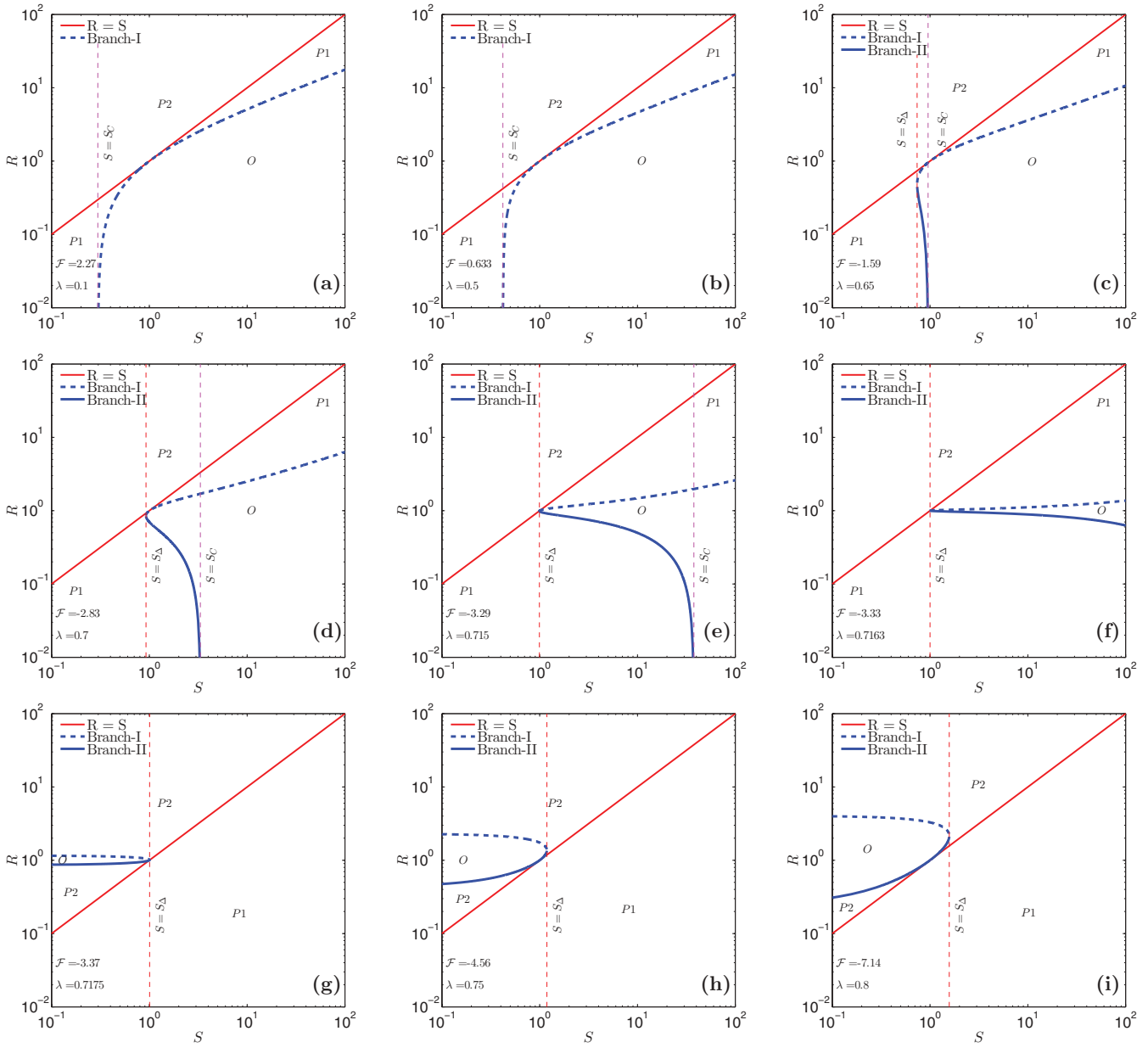

FIG. 11. (Color online) Evolution of the deformation-circulation map with the nondimensional domain size λ. Here, $\widetilde{\mu} = 0.3975$ and $\mathcal{F}_\infty = 2.2844$.

of Eqs. (12), (28), and (31), in conjunction with the detail of derivation of Eq. (23). This yields $\Phi = \Phi^e + \Phi^h$, where $\Phi^e \equiv R^2 + 1 - 2S$ and $\Phi^h \equiv (3/5)\mathcal{F}(R - S)$ represent, respectively, the contribution of the net normal electric and hydrodynamic stresses. Accordingly, $\mathcal{D}$ can be rewritten as $\mathcal{D} = \mathcal{D}^e + \mathcal{D}^h$, where $\mathcal{D}^e = (9\mathrm{Ca}_{el}/16)[\Gamma^2\Phi^e/(R+2)^2]$ and $\mathcal{D}^h = (9\mathrm{Ca}_{el}/16)[\Gamma^2\Phi^h/(R+2)^2]$. For a drop in an unbounded domain, $\mathcal{F}_\infty = (3\widetilde{\mu}+2)/(\widetilde{\mu}+1)$ is always positive, and therefore, the tendency of the net normal hydrodynamic stress $[\![\sigma^h_{rr}]\!]_\infty$ in setting the sense of drop deformation is solely determined by the sign of $R - S$. Here, $[\![\sigma^h_{rr}]\!]_\infty$ tends to deform the drop to a prolate in the $R > S$ region and to an oblate in the $R < S$ region. For a drop in a confined domain, however, this tendency depends on the sign of $\mathcal{F}(R - S)$ as $\mathcal{F}$ can be positive or negative (Fig. 8). For both bounded and unbounded domain, $[\![\tau^e_{rr}]\!]$ tends to deform the drop to a prolate for $R > S$, and to an oblate in nearly all the region identified by O in Fig. 10. Since Φ^e is quadratic in R, the contribution of $[\![\tau^e_{rr}]\!]$ compared to $[\![\sigma^h_{rr}]\!]$ is stronger in the $R > S$ region and weaker in the $R < S$ region.

A decrease in the domain size leads to a decrease in the magnitude of $\mathcal{F}$. While $\mathcal{F}$ is still positive, this leads to a decrease in the magnitude of $[\![\sigma^h_{rr}]\!]$ but does not affect its sign. Here, the decrease in the magnitude of $[\![\sigma^h_{rr}]\!]$ does not lead to a modification of the map in the $R > S$ region as $[\![\tau^e_{rr}]\!]$ also tends to deform the interface to a prolate in that region. However, the weakening of $[\![\sigma^h_{rr}]\!]$ affects the $R < S$ region since $[\![\sigma^h_{rr}]\!]$ is of the same order of or larger than $[\![\tau^e_{rr}]\!]$ in that region. This is the reason for the shrinkage of the oblate region in panel (b) relative to the same region in Fig. 10, which is noticeable but

not dramatic. Below a threshold domain size λ_0^{-1}, determined from $\mathcal{F} = 0$, $\mathcal{F}_{cr} < \mathcal{F} < 0$ and the shrinkage in the oblate region accelerates since the sign of $[\![\sigma^h_{rr}]\!]$ is reversed. This is seen in panels (c)–(f). From this point onward, $[\![\sigma^h_{rr}]\!]$ tends to deform the drop to an oblate in the $R > S$ region and to a prolate in the $R < S$ region. However, since $[\![\sigma^h_{rr}]\!]$ is not as strong as $[\![\tau^e_{rr}]\!]$, it does not affect the $R > S$ region. Below a critical domain size λ_{cr}^{-1}, determined from $\mathcal{F} = -10/3 \equiv \mathcal{F}_{cr}$, $\mathcal{F} < \mathcal{F}_{cr} < 0$ and $[\![\sigma^h_{rr}]\!]$ is sufficiently strong. Consequently, the net hydrodynamic stress leads to deformation of the drop to an oblate in some part of the $R > S$ region as shown in panels (g)–(i).

VI. CONCLUSION

The effect of a uniform electric field on steady-state behavior of a drop in a confined domain was investigated analytically. It was shown that the domain confinement led to the scaling of the electric potential ϕ_∞, the electric field $\mathbf{E}_\infty$, and the free electric surface charge q_{s_∞} by a correction factor Γ, where $\Gamma > 1$ for $R > 1$ and $\Gamma < 1$ for $R < 1$. On the other hand, the net electric stresses, $[\![\tau^e_{rr}]\!]_\infty$ and $[\![\tau^e_{r\theta}]\!]_\infty$, were scaled by Γ^2. The effect of confinement on the strength of the velocity field was investigated and it was shown that the flow strength, represented by the maximum surface velocity $U_{\max_\infty}$, was scaled by a correction factor $\Omega(R,\widetilde{\mu},\lambda)$, where Ω was a decreasing function of $\lambda = a/b$ for $R < 1$ while it grew with $\lambda = a/b$ for $R \gg 1$. The deformation of the drop was calculated posteriorly using a normal stress balance at the drop surface, and a zero-deformation curve $\Phi = 0$ was found, which delineated the region in the S-R space according to the sense of drop deformation. It was shown that the confinement effect could lead to the reversal of the tendency of the net normal hydrodynamic stress $[\![\sigma^h_{rr}]\!]$ in deforming the drop to an oblate or a prolate below a threshold domain size λ_0^{-1}, determined from $\mathcal{F} = 0$, and that below a critical domain size $\lambda_{cr}^{-1} < \lambda_0^{-1}$, determined from $\mathcal{F} = -10/3 \equiv \mathcal{F}_{cr}$, the necessary condition for having an oblate deformation would be $R > S$, which is the opposite to the corresponding condition for a drop in an unbounded domain, and also opposite to that for a drop in a confined domain where $\lambda < \lambda_{cr}$.

APPENDIX A: COEFFICIENTS USED IN THE SOLUTION OF THE STREAM FUNCTION

The following coefficients are used in the solution of the stream functions:

$$\Lambda_A(\lambda) = -20\lambda^{14} + 28\lambda^{12} - 58\lambda^7 + 70\lambda^5 - 20, \quad \text{(A1)}$$

$$\Lambda_B(\lambda) = 12\lambda^{12} - 20\lambda^{10} + 8\lambda^7 + 30\lambda^5 - 50\lambda^3 + 20, \quad \text{(A2)}$$

$$\Lambda_C(\lambda) = 8\lambda^{17} - 28\lambda^{12} + 40\lambda^{10} - 70\lambda^5 + 50\lambda^3, \quad \text{(A3)}$$

$$\Lambda_D(\lambda) = -8\lambda^{17} + 20\lambda^{14} - 12\lambda^{12} - 20\lambda^{10} + 50\lambda^7 - 30\lambda^5, \quad \text{(A4)}$$

and

$$\Lambda_E(\lambda) = 8\lambda^{17} - 50\lambda^{14} + 84\lambda^{12} - 30\lambda^{10} - 117\lambda^7 + 210\lambda^5 - 125\lambda^3 + 20. \quad \text{(A5)}$$

The above coefficients have the following attributes: (1) for $\lambda = 1$, all Λ's are zero, (2) in the limit of $\lambda \to 0$, $\Lambda_A = -20$, $\Lambda_B = 20$, $\Lambda_C = 0$, $\Lambda_D = 0$, and $\Lambda_E = 20$, (3) $\Lambda_B + \Lambda_A + \Lambda_C + \Lambda_D = 0$ as required by $u_{r_o}(a,\theta) = 0$, (4) $\Lambda_B\lambda^2 + \Lambda_A + \Lambda_C/\lambda^3 + \Lambda_D/\lambda^5 = 0$ as required by $u_{r_o}(b,\theta) = 0$, (5) $2\Lambda_B\lambda^4 - 3\Lambda_C/\lambda - 5\Lambda_D/\lambda^3 = \Lambda_E$ as required by $u_\theta(a,\theta) = U_{\max}\sin 2\theta$.

APPENDIX B: SUMMARY OF THE RESULTS FOR HYDRODYNAMICS OF A DROP IN AN UNBOUNDED DOMAIN

For a drop in an unbounded domain, the stream functions are

$$\frac{\psi_{i_\infty}}{U_{\max_\infty} a^2} = \left[\left(\frac{r}{a}\right)^3 - \left(\frac{r}{a}\right)^5\right]\sin^2\theta\cos\theta \quad \text{(B1)}$$

and

$$\frac{\psi_{o_\infty}}{U_{\max_\infty} a^2} = \left[\left(\frac{a}{r}\right)^2 - 1\right]\sin^2\theta\cos\theta, \quad \text{(B2)}$$

where the maximum velocity $U_{\max_\infty}$ is as given in Eq. (21). The velocities are

$$\frac{u_{r_{i\infty}}}{U_{\max_\infty}} = \left[\left(\frac{r}{a}\right)^3 - \left(\frac{r}{a}\right)\right](1 - 3\cos^2\theta), \quad \text{(B3)}$$

$$\frac{u_{\theta_{i\infty}}}{U_{\max_\infty}} = \frac{1}{2}\left[5\left(\frac{r}{a}\right)^3 - 3\left(\frac{r}{a}\right)\right]\sin 2\theta, \quad \text{(B4)}$$

$$\frac{u_{r_{o\infty}}}{U_{\max_\infty}} = \left[\left(\frac{a}{r}\right)^2 - \left(\frac{a}{r}\right)^4\right](1 - 3\cos^2\theta), \quad \text{(B5)}$$

and

$$\frac{u_{\theta_{o\infty}}}{U_{\max_\infty}} = \left(\frac{a}{r}\right)^4 \sin 2\theta. \quad \text{(B6)}$$

The jump in the pressure is

$$\frac{[\![p]\!]_\infty}{\mu_o U_{\max}/a} = (2 - 7\widetilde{\mu})(1 - 3\cos^2\theta), \quad \text{(B7)}$$

and the jump in the deviatoric normal hydrodynamic stress is as given in Eq. (26), yielding the jump in the normal hydrodynamic stress

$$\frac{[\![\sigma^h_{rr}]\!]_\infty}{\mu_o U_{\max_\infty}/a} = (3\widetilde{\mu} + 2)(1 - 3\cos^2\theta). \quad \text{(B8)}$$

The net hydrodynamic shear stress is $[\![\tau^h_{r\theta}]\!]_\infty = -[\![\tau^e_{r\theta}]\!]_\infty$, as required by the tangential stress balance at the interface.

[1] W. A. Macky, Proc. R. Soc. London A **133**, 565 (1931).
[2] C. G. Garton and Z. Krasucki, Proc. R. Soc. London A **280**, 211 (1964).
[3] F. A. Morrison, Trans. ASME: J. Heat Transfer **99**, 269 (1977).
[4] T. B. Jones, Adv. Heat Trans. **14**, 107 (1978).

[5] K. J. Ptasinski and P. J. A. M. Kerkhof, Sep. Sci. Technol. **27**, 995 (1992).
[6] A. Banerjee, E. Kreit, Y. Liu, J. Heikenfeld, and I. Papautsky, Lab Chip **12**, 758 (2012).
[7] K. Ikemoto, I. Sakata, and T. Sakai, Sci. Rep. **2**, 289 (2012).
[8] M. R. Abdelaal and M. A. Jog, Int. J. Heat Mass Transf. **55**, 251 (2012).
[9] C. T. O'Konski and H. C. Thacher, J. Phys. Chem. **57**, 955 (1953).
[10] C. T. O'Konski and F. E. Harris, J. Phys. Chem. **61**, 1172 (1957).
[11] R. S. Allan and S. G. Mason, Proc. R. Soc. London A **267**, 45 (1962).
[12] G. I. Taylor, Proc. R. Soc. London A **280**, 383 (1964).
[13] C. E. Rosenkilde, Proc. R. Soc. London A **312**, 473 (1969).
[14] G. I. Taylor, Proc. R. Soc. London A **291**, 159 (1966).
[15] O. Vizika and D. A. Saville, J. Fluid Mech. **239**, 1 (1992).
[16] G. I. Taylor, Proc. R. Soc. London A **146**, 501 (1934).
[17] T. Tsukada, T. Katayama, Y. Ito, and M. Hozawa, J. Chem. Eng. Jpn. **26**, 698 (1993).
[18] J. Q. Feng and T. C. Scott, J. Fluid Mech. **311**, 289 (1996).
[19] J. Q. Feng, Proc. R. Soc. London A **455**, 2245 (1999).
[20] S. Torza, R. G. Cox, and S. G. Mason, Philos. Trans. R. Soc. London A **269**, 295 (1971).
[21] C. T. R. Wilson and G. I. Taylor, Proc. Cambridge Philos. Soc. **22**, 728 (1925).
[22] J. D. Sherwood, J. Fluid Mech. **188**, 133 (1988).
[23] N. Bentenitis and S. Krause, Langmuir **21**, 6194 (2005).
[24] E. Lac and G. M. Homsy, J. Fluid Mech. **590**, 239 (2007).
[25] D. A. Saville, Annu. Rev. Fluid Mech. **29**, 27 (1997).
[26] P. A. Arp, R. T. Foister, and S. G. Mason, Adv. Colloid Interface Sci. **12**, 295 (1980).
[27] J. R. Melcher and G. I. Taylor, Annu. Rev. Fluid Mech. **1**, 111 (1969).
[28] M. N. Reddy and A. Esmaeeli, Int. J. Multiphase Flow **35**, 1051 (2009).
[29] J. C. Baygents, J. J. Rivette, and H. A. Stone, J. Fluid Mech. **368**, 359 (1998).
[30] T. Tsukada, Y. Yamamoto, T. Katayama, and M. Hozawa, J. Chem. Eng. Jpn. **27**, 662 (1994).
[31] D. Eisenberg and W. Kauzmann, *The Structure and Properties of Water* (Oxford University Press, New York, 1969).
[32] L. G. Hector and H. L. Schultz, J. Appl. Phys. **7**, 133 (1936).
[33] A. Esmaeeli and P. Sharifi, Phys. Rev. E **84**, 036308 (2011).